

THE GLAM AIRBORNE CAMPAIGN ACROSS THE MEDITERRANEAN BASIN

PHILIPPE RICAUD, RÉGINA ZBINDEN, VALÉRY CATOIRE, VANESSA BROCCHI, FRANÇOIS DULAC, ERIC HAMONOU, JEAN-CHRISTOPHE CANONICI, LAAZIZ EL AMRAOUI, SÉBASTIEN MASSART, BRUNO PIGUET, URI DAYAN, PIERRE NABAT, JEAN SCIARE, MICHEL RAMONET, MARC DELMOTTE, ALCIDE DI SARRA, DAMIANO SFERLAZZO, TATIANA DI IORIO, SALVATORE PIACENTINO, PAOLO CRISTOFANELLI, NIKOS MIHALOPOULOS, GIORGOS KOUVARAKIS, MICHAEL PIKRIDAS, CHRYSANTHOS SAVVIDES, RODANTHI-ELISAVET MAMOURI, ARGYRO NISANTZI, DIOFANTOS HADJIMITSIS, JEAN-LUC ATTIE, HÉLÈNE FERRÉ, YANNICK KANGAH, NIZAR JAIDAN, JONATHAN GUTH, PATRICK JACQUET, STÉPHANE CHEVRIER, CLAUDE ROBERT, AURÉLIEN BOURDON, JEAN-FRANÇOIS BOURDINOT, JEAN-CLAUDE ETIENNE, GISÈLE KRYSZTOFIK, AND PIERRE THERON

The Gradient in Longitude of Atmospheric Constituents above the Mediterranean Basin (GLAM) 2014 airborne campaign performed original in situ observations of gases and aerosols across the Mediterranean troposphere, which, combined with satellite measurements and model outputs, highlight their summertime variability.

The Mediterranean is located in a transitional zone between subtropical and midlatitude regimes (Lionello 2012) and is highly sensitive to climate change. Global and regional model simulations show a pronounced decrease in precipitation (2000–2100), especially during the warm season (Giorgi and Lionello 2008). Observations over the last few decades show a similar decrease in precipitation (Shohami et al. 2011). In terms of anthropogenic pollution sources, the eastern Mediterranean is at the crossroads between four continents (North America, Europe, Africa, and Asia). The impact of these various continental sources, which include industrial and densely populated coastal areas (Kanakidou et al. 2011; Im and Kanakidou 2012) as well as forest fires (Pace et al. 2005; Cristofanelli et al. 2013), is still not fully understood, particularly when considering the

ozone (O_3) and carbon monoxide (CO) budgets in which methane (CH_4) plays an interactive role by way of its complex reactions with nitrogen oxides (NO_x ; Dentener et al. 2005). Polluted air masses may originate from Europe (e.g., Pace et al. 2006), Asia (e.g., Lelieveld et al. 2002; Randel and Park 2006), Africa (e.g., Ziv et al. 2004; Liu et al. 2009), or even North America (e.g., Forster et al. 2001; Formenti et al. 2002; Christoudias et al. 2012). Data from satellite observations and model outputs (e.g., Lelieveld et al. 2002; Nabat et al. 2013), reviewed in combination with measurements collected by campaigns such as the Mediterranean Intensive Oxidant Study (MINOS; Ladstätter-Weissenmayer et al. 2003; Scheeren et al. 2003), reveal that during the warm and dry summer season, air pollution above the Mediterranean often exceeds the concentrations observed over most of

the rest of Europe. This is due to the convergence of European, African, and Asian polluted air masses, the absence of rain to cleanse the atmosphere, and the high insolation that favors the formation of secondary pollutants such as ultrafine particles or ozone. Aerosol pollution might originate from various natural sources such as the African and Arabian deserts, active volcanoes, vegetation, or the sea surface. The summer Asian monsoon convection can lift greenhouse gases, pollutants, and aerosols originating in Asia up to the upper troposphere, where they are then carried toward the eastern Mediterranean basin by the Asian monsoon anticyclone. Once there, they accumulate and are subject to subsidence (Ricaud et al. 2014; Dayan et al. 2017).

Based on measurements from spaceborne instruments and outputs from chemistry–climate and chemistry–transport models, Ricaud et al. (2014) have shown that the atmospheric conditions in the western Mediterranean basin favor enrichment, for instance in CH_4 , which contrast with conditions in the eastern basin, as shown by the pioneering study carried out by Lelieveld et al. (2002). The reason for this is due to the dominant winds blowing from the west and Europe. This is true of almost all seasons and altitudes, apart from summer in the mid- to upper troposphere at altitudes between 5 and 9 km. In summer, pollutants (including CH_4) are trapped by the subsiding air masses that form part of the Asian monsoon anticyclone and driven toward the eastern Mediterranean basin, where they produce a strong local maximum. Kangah et al. (2017) looked

at another long-lived species: nitrous oxide (N_2O). Using spaceborne measurements, they were able to demonstrate the summertime enrichment of N_2O over the eastern Mediterranean basin, which is consistent with the increase in surface emissions and convective precipitation over the Indian subcontinent during the summer monsoon period. They state that N_2O over the eastern Mediterranean basin could be seen as the footprint of Asian summertime emissions.

The aim of the Gradient in Longitude of Atmospheric Constituents above the Mediterranean Basin (GLAM) airborne experiment was to document the east–west summertime gradients in atmospheric pollutants, including greenhouse gases and aerosols, in the lower atmosphere of the Mediterranean basin. The chosen period allowed for particular focus on the impact of the Asian monsoon on the air composition of the mid- and upper troposphere in the eastern section of the Mediterranean basin. In this part of the basin, in summer, pollutants and greenhouse gases measured by spaceborne instruments or calculated using models show strong spatial and temporal variability. In addition, we also explored the marine boundary layer over this part of the basin to produce a three-dimensional structure of the volume mixing ratios of the chemical compounds from the lowermost to the uppermost (~12 km) troposphere.

The airborne campaign took place between 6 and 10 August 2014. It followed an east–west flight path from France to Cyprus and gathered data using instruments on board the Falcon-20 (F-20)

AFFILIATIONS: RICAUD, ZBINDEN, EL AMRAOUI, PIGUET, NABAT, KANGAH, JAIDAN, GUTH, AND THERON—Météo-France, CNRM/CNRS, UMR 3589, Toulouse, France; CATOIRE, BROCCHI, JACQUET, CHEVRIER, ROBERT, AND KRYSZTOFIK—LPC2E, UMR 7328 CNRS-Université d'Orléans, France; DULAC, HAMONOU, RAMONET, AND DELMOTTE—Laboratoire des Sciences du Climat et de l'Environnement, LSCE/IPSL, CEA-CNRS-UVSQ, Université Paris-Saclay, Gif-sur-Yvette, France; CANONICI, BOURDON, BOURDINOT, AND ETIENNE: SAFIRE, Toulouse, France; MASSART—European Centre for Medium-Range Weather Forecasts, Reading, United Kingdom; DAYAN—Hebrew University of Jerusalem, Jerusalem, Israel; SCIARE AND PIKRIDAS—Energy Environment Water Research Centre, Cyprus Institute, Nicosia, Cyprus; MAMOURI—Energy Environment Water Research Centre, Cyprus Institute, Nicosia, and Cyprus University of Technology, Department of Civil Engineering and Geomatics, Limassol, Cyprus; DI SARRA, SFERLAZZO, DI IORIO, AND PIACENTINO—Italian National Agency for New Technologies, Energy and Sustainable Economic Development (ENEA), Rome, Italy; CRISTOFANELLI—Institute of Atmospheric Sciences and Climates (ISAC)/National Research Council of Italy (CNR), Bologna, Italy; MIHALOPOULOS AND KOUVARAKIS—Environmental Chemical Processes

Laboratory, Department of Chemistry, University of Crete, Voutes, Heraklion, Greece; SAVVIDES—Air Quality Section, Department of Labour Inspection, Nicosia, Cyprus; NISANTZI AND HADJIMITSIS—Department of Civil Engineering and Geomatics, Cyprus University of Technology, Limassol, Cyprus; ATTÍE—University of Toulouse, Laboratoire d'Aérodynamique, UMR 5560, Toulouse, France; FERRÉ—Service de Données de l'Omp, Observatoire Midi-Pyrénées, Toulouse, France

CORRESPONDING AUTHOR: Philippe Ricaud, philippe.ricaud@meteo.fr

The abstract for this article can be found in this issue, following the table of contents.

DOI:10.1175/BAMS-D-16-0226.1

In final form 13 July 2017

©2018 American Meteorological Society

For information regarding reuse of this content and general copyright information, consult the [AMS Copyright Policy](#).



This article is licensed under a [Creative Commons Attribution 4.0 license](#).

aircraft belonging to the Service des Avions Français Instrumentés pour la Recherche en Environnement (SAFIRE). The onboard equipment consisted primarily of a laser infrared spectrometer [Spectromètre InfraRouge In situ Toute altitude (SPIRIT)], which was able to measure CO, carbon dioxide (CO₂), CH₄, and N₂O as well as take additional measurements of aerosols, water vapor (H₂O), and O₃. The flight cruising altitude was 5,425 ± 55 m above mean sea level (MSL) on the outbound journey from Toulouse (France) to Larnaca (Cyprus) via Minorca (Spain), Lampedusa (Italy), and Heraklion (Crete) and 9,680 ± 50 m MSL on the return leg. Vertical profiles from the surface to about 12 km MSL were collected near the four landing sites (Minorca, Lampedusa, Heraklion, and Larnaca), and additional atmospheric profiles were generated and intermediate altitude transects performed south of Larnaca. Note that all profiles, except those gathered above Minorca, allow for comparison with the local routine monitoring measurements (surface and vertical profiles) taken at Lampedusa, Finokalia, and Cyprus. Forecasts and analyses obtained from the Copernicus Atmosphere Monitoring Service (CAMS; <https://atmosphere.copernicus.eu>) operated by the European Centre for Medium-Range Weather Forecasts (ECMWF), as well as other model outputs and satellite observations, were used to interpret the GLAM campaign's measurements and quantify the impact of local sources versus long-range transport on the east–west gradient of atmospheric constituents by relevant altitude. In this paper, we describe the GLAM airborne campaign, the datasets provided, and some of its findings, most of which focus on the long-range transport of pollutants (O₃, CO), greenhouse gases (CH₄, CO₂), and aerosols. Particular emphasis has been given to the east–west variability of pollutants and greenhouse gases in the midtroposphere and the surface measurements of aerosols.

OVERVIEW OF THE GLAM EXPERIMENTAL

DESIGN. *The airborne in situ measurements.* The SPIRIT instrument on board the F-20 was operated by a team from the Laboratoire de Physique et Chimie de l'Environnement et de l'Espace (LPC2E), while the SAFIRE team operated the remaining instruments. Position, orientation, and speed were measured using a GPS-coupled inertial navigation system. Water vapor was measured using three different instruments: a capacitive thin-film sensor (Aerodata), which primarily measured relative humidity; a chilled mirror hygrometer (CR-2 model from Buck Research), which provided a dewpoint or

frost point temperature; and a tunable diode laser absorption spectroscopy hygrometer (WVSS-II from SpectraSensors). Ozone concentration was measured using the Mozart instrument, which is a modified version of a commercial ozone analyzer (TEI 49C), itself an early version of the instrument used for the Measurement of Ozone by Airbus In-Service Aircraft (MOZAIC) program (Marenco et al. 1998). Mozart's one-sigma (1σ) measurement accuracy is identical to the 1σ accuracy of the MOZAIC instruments, which has been estimated at ±[2 ppbv + 2%] (Thouret et al. 1998). The size-distributed number concentration of aerosol particles was provided by two optical spectrometers manufactured by Droplet Measurement Technologies (DMT): a passive cavity aerosol spectrometer probe (PCASP), measuring particles within the 0.095–3.1-μm-diameter range into 30 bins, and an ultra-high-sensitivity aerosol spectrometer (UHSAS-A), measuring particles within the 0.04–1.0-μm-diameter range into 99 bins. Both the PCASP and UHSAS-A instruments were mounted outside the aircraft, below the wings, and were consequently flown in the free airstream.

SPIRIT is an airborne infrared absorption spectrometer that can carry out the simultaneous measurement of several trace gases (McQuaid et al. 2013). It uses three continuous wave, distributed feedback, room temperature quantum cascade lasers (QCLs), allowing ultra-high spectral resolution (10⁻³ cm⁻¹) and for the scanning of the strong fundamental molecular ro-vibrational lines found in the midinfrared. During the GLAM campaign, measurements were taken at the following wavenumbers: 2,179.772 cm⁻¹ for ¹²C¹⁶O, 1,249.627 cm⁻¹ for ¹²C¹H₄, 1,249.668 cm⁻¹ for ¹⁴N₂¹⁶O, and 2,307.513 cm⁻¹ for ¹²C¹⁸O¹⁶O. Total molecule abundances were calculated from the isotopic ratios reported in the High-Resolution Transmission (HITRAN) 2012 database (Rothman et al. 2013). The dry volume mixing ratios of the trace gases were calculated using optical cell pressure and temperature measurements (Guimbaud et al. 2011), and the water vapor mixing ratios were measured using either the WVSS-II hygrometer or SPIRIT. By comparing the data collected during other flights with those obtained from high-altitude instrumented surface stations belonging to the World Meteorological Organization/Global Atmosphere Watch network (Pic du Midi de Bigorre and Puy de Dôme, France), total 1σ uncertainties are estimated at ±4 ppbv for CO (at ~120 ppbv), that is, ~3.4%; ±8 ppmv for CO₂ (at ~395 ppmv), that is, ~2%; ±20 ppbv for CH₄ (at ~1,900 ppbv), that is, ~1.1%; and ±15 ppbv for N₂O (at ~325 ppbv), that is, ~4.5%.

TABLE I. Dates, locations, and altitudes of the flights made during the GLAM airborne campaign.

Date	Flight No. ^a	Type	Start		End	
			Time (UTC)	Location	Time (UTC)	Location
6 Aug 2014	F1	Transect (alt: 5.4 km)	0714:01	Toulouse	0814:02	Minorca
	P1	Profile 0–12.2 km	0836:58	Minorca	0910:36	Minorca (landing: 0920:54 UTC)
	F2	Transect (alt: 5.4 km)	1110:43	Minorca	1248:00	Lampedusa
	P2	Profile 0–12.2 km	1311:05	Lampedusa	1352:27	Lampedusa
	F3	Transect (alt: 5.4 km)	0730:26	Lampedusa	0830:27	Heraklion
	P3	Profile 0–12.8 km	0957:14	Heraklion	1047:16	Heraklion
7 Aug 2014	F4	Transect (alt: 5.4 km)	1234:20	Heraklion	1334:21	Cyprus (near Paphos)
	P4	Profile 0–11.6 km	1423:00	Cyprus (near Tobal)	1500:50	Cyprus (near Tobal; northwest of Paphos)
	F4	Transect (alt: 3.0 km)	1500:50	Cyprus (Tobal)	1536:14	Larnaca
	F5	Transect (alt: 0.3 km)	1004:55	Larnaca	1104:56	Larnaca
8 Aug 2014	P5	Profile 0–13.0 km	1202:30	35.00°N, ~34.75°E	1244:28	35.00°N, ~34.75°E
	F6	Transect (alt: 5.4 km)	1443:55	Larnaca	1643:56	Larnaca
	P6	Profile 0–13.0 km	1652:18	APLON 33.15°N, 32.10°E	1729:39	APLON 33.15°N, 32.10°E
	Day off					
10 Aug 2014	F7	Transect (alt: 9.7 km)	0704:28	Larnaca	1016:35	Lampedusa
	F8	Transect (alt: 9.7 km)	1213:14	Lampedusa	1432:44	Toulouse

^a Only six vertical profiles (P1–P6) reaching an altitude of ~12 km are listed. Further vertical profiles were collected between either take off and the transect altitude (5.4 or 9.7 km) or the transect altitude and landing but are not shown here.

The airborne campaign. A list of the dates, locations, and altitudes of the eight flights made by the F-20 between 6 and 8 August, as well as on 10 August 2014, are provided in Table 1. A map of the flight paths is also provided in Fig. 1. The purpose of GLAM was to follow a west to east transect at an altitude of ~5 km (midtroposphere) on 6–7 August and a return east-to-west transect at an altitude of ~9 km (upper troposphere) on 10 August, with vertical profiles (0–12 km) collected in the vicinity of the landing airports. One day (8 August) was also spent taking samples in the easternmost Mediterranean basin between the maritime boundary layer and the upper troposphere. On 6 August, two west-to-east flights were made: from Toulouse to Minorca (flight 1 or F1) with a profile (P1) collected above Minorca before landing and from Minorca to Lampedusa (flight 2 or F2) with a profile (P2) collected above Lampedusa before landing. On 7 August, two more west-to-east flights were made: from Lampedusa to Heraklion (flight 3 or F3) with a profile (P3) collected above Heraklion before landing and from Heraklion to Larnaca (flight 4 or F4) with a profile (P4) collected off the western coast of Cyprus before landing. On 8 August, two flights were made: i) off the southern coast of Larnaca in the maritime boundary layer (flight 5 or F5) with a profile (P5) collected off the eastern coast of Cyprus and ii) off the southern coast of Larnaca in the free and upper troposphere (flight 6 or F6) with a profile (P6) collected off the southern coast of Cyprus before landing. On 10 August, two east-to-west flights were made: from Larnaca to Lampedusa (flight 7 or F7) and from Lampedusa to Toulouse (flight 8 or F8). In the descending phase, the ground track of the F-20 profiles (P1–P6) covered an area smaller than $0.3^{\circ} \times 0.3^{\circ}$ (latitude by longitude) and generally ended near the sea surface. In the ascending phase, the partial profiles P1–P4 began at an altitude of around 5 km, P5 began at 0.3 km, and P6 began at about 9.7 km. In addition to these dedicated profiles collected while the aircraft was ascending/descending in spirals, some vertical excursions performed along the flight route (between



FIG. 1. Schematic diagram of GLAM campaign flights, transects, and vertical profiles. The red lines represent flights from Toulouse to Larnaca at an altitude of 5 km, while the green lines represent flights from Larnaca to Toulouse at an altitude of 9 km. The blue lines show the flights in the vicinity of Larnaca at altitudes of 300, 5,000, and 9,000 m. Vertical profiles captured between an altitude of ~12-km altitude and the surface are represented by a spiral.

takeoff and transit altitude and between transit altitude and landing) provided more information on the vertical profiles and have also been considered in this analysis. All the GLAM airborne data are freely available online (at http://mistrals.sedoo.fr/?q=glam&project_name=ChArMEx). Any user can access the GLAM data after being registered to the Mediterranean Integrated Studies at Regional And Local Scales (MISTRALS)/Chemistry–Aerosol Mediterranean Experiment (ChArMEx) database.

The pre- and postanalysis of the model experimental design. Prior to and during the GLAM campaign, on the day before each flight, chemical and meteorological forecasts were provided by CAMS (chemical forecasts; Agustí-Panareda et al. 2014; Inness et al. 2015) and Météo-France (meteorological forecasts; Courtier et al. 1991). After the GLAM campaign, chemical and meteorological analyses were performed and comparisons were made between GLAM in situ data and satellite and surface measurements as well as chemical and meteorological analyses.

Based on the Composition-Integrated Forecasting System (C-IFS), CAMS/C-IFS provides real-time information and forecasts of the main atmospheric tracers (including CO₂, CH₄, O₃, CO, and aerosols) at global and regional scales (Massart et al. 2014, 2016; Benedetti et al. 2009; Inness et al. 2015). In this paper, we use O₃ and CO analyses provided on a reduced linear Gaussian grid (N80, resolution of about 1.125° × 1.125°) and 60 vertical levels between the surface and 0.1 hPa. We also use CO₂ and CH₄

analyses provided on a reduced linear Gaussian grid (N256, resolution of about $0.70^\circ \times 0.70^\circ$). As an example, in Fig. 2, we have provided the forecast fields of pollutants (O_3 and CO) and greenhouse gases (CO_2 and CH_4) calculated by CAMS/C-IFS at 500 hPa at 1200 UTC on 6 August 2014. These forecasts were used for the first two flights (F1 and F2) as well as the F-20 flight track between Toulouse and Lampedusa.

Another model used in our study was Modèle de Chimie Atmosphérique à Grande Echelle (MOCAGE; Peuch et al. 1999). It is a 3D chemistry transport model (CTM) that simulates the atmosphere between the planetary boundary layer and the stratosphere. MOCAGE is forced dynamically by external wind and temperature fields using analyses provided by Météo-France's operational model Action de Recherche Petite Echelle Grande Echelle (ARPEGE; Courtier et al. 1991). MOCAGE was run over a regional nested domain centered on the Mediterranean basin at a horizontal resolution of $0.2^\circ \times 0.2^\circ$ forced on its boundaries by a $2^\circ \times 2^\circ$ global domain, with 25 levels in the vertical domain of the GLAM measurements. In terms of emission inventories for chemical species for the global domain, we used the Global Emissions Initiative (GEIA; Guenther et al. 1995) inventory for natural emissions and the inventory developed by Lamarque et al. (2010) for the anthropogenic emissions. For the regional domain, we used the Monitoring Atmospheric Composition and Climate—Interim Implementation (MACC-II) inventory (Kuenen et al. 2011) for the anthropogenic emissions, the Global Fire Assimilation System (GFAS_1.1) product (Kaiser et al. 2012) for biomass burning emissions, and the GEIA inventory for

natural emissions. The MOCAGE model for aerosols was run independently from the simulation for chemical species. MOCAGE contains four primary aerosol species: desert dust (DD), sea salt (SS), black carbon (BC), and organic carbon (OC). A detailed description of all the aerosol parameterizations and emissions used in the MOCAGE model can be found in Sič et al. (2015).

Aire Limitée Adaptation Dynamique Développement International (ALADIN)-Climate is a regional climate model based on a bispectral, semi-implicit, semi-Lagrangian scheme. Version 5.3 (Nabat et al. 2015) was also used for the purposes of this study, with a 50-km horizontal resolution and 31 vertical levels. The model includes a prognostic aerosol scheme, adapted from the Global and Regional Earth-System (Atmosphere) Monitoring Using Satellite and In situ Data (GEMS) and MACC aerosol scheme (Morcrette et al. 2009; Benedetti et al. 2011; Michou et al. 2015). The aerosol species represented are dust, sea salt, sulfate, black carbon, and organic particles. The spatial domain of our simulations was designed to include all possible sources generating aerosols that could be transported over the Mediterranean basin, such as dust particles from the Saharan Desert and sea salt aerosols from the northern Atlantic Ocean. Further information on the aerosol scheme, as well as an evaluation of its performance, can be found in Nabat et al. (2015).

To follow the history of the air parcels sampled during the GLAM campaign's transects and measurement of profiles at a particular geographic position (latitude, longitude, and pressure), back and forward trajectories were analyzed using the British

Atmospheric Data Centre (BADC) Web Trajectory Service (<http://badc.nerc.ac.uk/community/trajectory/>), which is based on ECMWF analyses. We used ECMWF archives (2.5° resolution) with pressure vertical coordinates and selected the pressure vertical velocity for the vertical advection, with 1-h frequency over a 10-day period.

Air parcel trajectories were also simulated using the Flexible Particle (FLEXPART) dispersion model (see www.flexpart.eu/; Stohl et al.

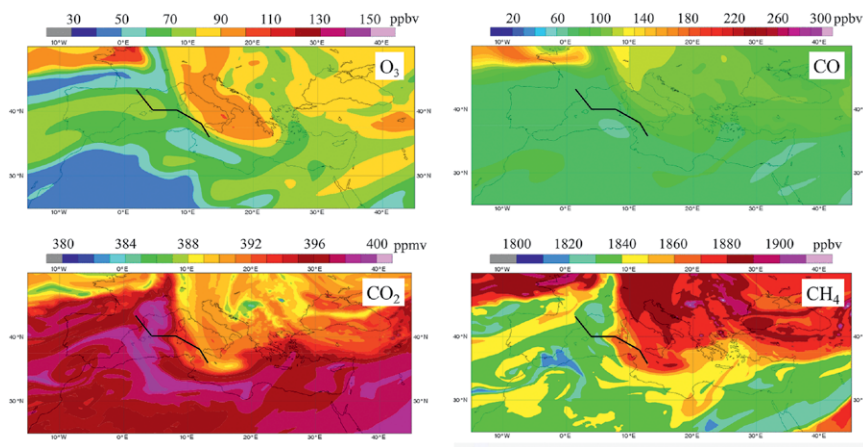


FIG. 2. Longitude–latitude cross sections of (top left) O_3 , (top right) CO , (bottom left) CO_2 , and (bottom right) CH_4 forecasts generated by CAMS/C-IFS at 1200 UTC 6 Aug 2014 at 500 hPa calculated at 0000 UTC 4 Aug 2014 available for the first two flights (F1 and F2, flight track represented by thick black line) between Toulouse and Lampedusa.

2005). The 20-day backward calculations (Seibert and Frank 2004) were performed along the flight track and are presented in Brocchi et al. (2017, manuscript submitted to *Atmos. Chem. Phys. Discuss.*). For the meteorological fields, the input parameters from ECMWF as, for example, horizontal and vertical winds and temperature were used, with a horizontal resolution of $0.5^\circ \times 0.5^\circ$ and 137 model levels. Every simulation consisted of 20,000 particles released at the flight location with full transport parameterization settings on. Aerosols were first simulated as a passive tracer without removal processes, and next by assuming a decreasing concentration of aerosols caused by dry and wet deposition. Aerosol-like transport properties were assumed to be similar to those of BC. Emission sensitivities for both simulations were extracted by multiplying the footprint (emission sensitivity) by the emission fluxes for dust from the Sahara and BC from biomass burning. In terms of emission inventories, the GFAS inventory was used for BC, and MOCAGE outputs were used for DD.

Finally, the Hybrid Single Particle Lagrangian Integrated Trajectory (HYSPPLIT) model (see <http://ready.arl.noaa.gov/HYSPLIT.php>; Stein et al. 2015) was used to calculate 20-day back trajectories for the air parcels along the transect to assess their origins. These trajectories were calculated using global reanalysis data archives provided by the National Oceanic and Atmospheric Administration (NOAA)'s National Centers for Environmental Prediction–National Center for Atmospheric Research (NCEP–NCAR) as the meteorological data input to the model. The global reanalyses are on a latitude–longitude grid of $2.5^\circ \times 2.5^\circ$.

The satellite data. We studied spaceborne O_3 products assimilated from the Ozone Monitoring Instrument (OMI) and Microwave Limb Sounder (MLS), aerosol products from *Cloud–Aerosol Lidar and Infrared Pathfinder Satellite Observations* (CALIPSO), Moderate Resolution Imaging Spectroradiometer (MODIS), Spinning Enhanced Visible and Infrared Imager (SEVIRI), and Atmospheric Infrared Sounder (AIRS), and fire products from MODIS. Tropospheric ozone was examined using the ozone products derived from the visible and UV nadir-scanning OMI and the MLS on board the *Aura* satellite, which were assimilated into the Goddard Earth Observing System, version 5 (GEOS-5), data assimilation system (Ziemke et al. 2014; Wargan et al. 2015). The assimilated products were generated for 72 atmospheric levels with a $2.0^\circ \times 2.5^\circ$ horizontal resolution. For the purposes of the GLAM campaign,

only the 35 lowest layers were investigated to cover the lowermost troposphere up to about 100 hPa. The MODIS instruments on board the *Terra* and *Aqua* platforms were used to detect fire, smoke, cloud, and aerosols. Data obtained from NASA's Earth Observing System Data and Information System (EOSDIS) Worldview, version 0.9.0. (<https://earthdata.nasa.gov/worldview>), were used to identify fire occurrences. To highlight aerosols, this study used the dust score derived from day and night overpasses by the AIRS on board the *Aqua* platform, using Level1B AIRIBQAP_NRT data (https://cmr.earthdata.nasa.gov/search/concepts/C1233768981-GES_DISC.html), which indicated high levels of aerosols in Earth's atmosphere. The aerosol optical depth obtained from MODIS on *Aqua* and *Terra* was also used. The CALIPSO satellite, part of the international A-Train constellation, provided the 532-nm total (parallel and perpendicular) attenuated backscatter aerosol and vertical feature mask, retrieved from the NASA CALIPSO web page (<http://www-calipso.larc.nasa.gov/products/lidar/>). The SEVIRI instrument on board the Meteosat Second Generation (MSG) *Meteosat-10* geostationary platform provided the aerosol optical depth at 550 nm (AOD_{550}) over the sea. AOD_{550} was operationally produced in near-real time using European Organisation for the Exploitation of Meteorological Satellites (EUMETSAT) data obtained from the Cloud-Aerosol-Water-Radiation Interactions (ICARE) data and service center (see www.icare.univ-lille.fr/msg/browse/; Thieuleux et al. 2005). For further information, we also used “natural” and “dust” false-color composite images produced by EUMETSAT (<http://oiswww.eumetsat.org/IPPS/html/MSG/RGB/>), which combine coincident images from several channels into a red–green–blue composition in order to highlight clouds and dust plumes. Near-real-time quick looks were available online during the campaign on the ChArMEx Operation Center server (<http://choc.sedoo.fr>).

The surface measurements. Table 2 lists the six surface background stations (located on three Mediterranean islands) where chemical species and aerosols were measured along the flight track during the GLAM campaign, either in situ at the surface or remotely in the atmosphere using active and passive techniques. The stations are located in Lampedusa, Italy (World Meteorological Organization/Global Atmosphere Watch regional station); Finokalia, Crete, Greece (European Monitoring and Evaluation Programme station and Aerosols, Clouds, and Trace Gases Research Infrastructure); and in Cyprus (air quality stations

TABLE 2. Surface stations and instruments used during the GLAM airborne campaign.

Country	Stations	Latitude (°N)	Longitude (°E)	Altitude (m MSL)	Instruments	Species
Italy	Lampedusa Island	35.52	12.63	45	Air quality	O ₃
					Picarro	CO
					Picarro	CH ₄
					Picarro	CO ₂
					Lidar	Aerosols
Crete Island, Greece	Finokalia	35.33	25.67	250	Air quality	O ₃
					Picarro	CO
					Picarro	CH ₄
					Picarro	CO ₂
					Scanning mobility particle sizer	Aerosols
Cyprus	Agia Marina-Xyliatou	35.03	33.05	520	Air quality	O ₃
	Ineia	34.96	32.40	665	Air quality	O ₃
	Troodos	34.94	32.87	1,819	Air quality	O ₃
	Limassol	34.68	33.04	10	Lidar	Aerosols

belonging to the Environmental Protection Agencies: Ineia, near the west coast; Agia Marina-Xyliatou, in the central region; Troodos in the central and elevated regions; and Limassol, on the south coast).

SCIENTIFIC OUTCOMES. To make the different datasets consistent and comparable, the volume mixing ratios of the chemical species measured during the GLAM campaign are all expressed in parts per billion by volume (ppbv) [or parts per million by volume (ppmv) for CO₂] with respect to dry air.

Intercontinental transport. We highlight here intercontinental transport processes based on two different analyses over the western and eastern Mediterranean. The first analysis over the western Mediterranean relies on measurements taken during the last flight on 10 August along the 9-km transect between Lampedusa and Toulouse, when episodes of intense aerosol loading were detected. The second analysis over the eastern Mediterranean is based on pollutant and greenhouse gas vertical profiles measured on 8 August in the upper troposphere off the coast of Cyprus.

WESTERN MEDITERRANEAN. During the last flight (F8) along the 9-km transect on 10 August, two episodes of intense aerosol loadings were detected between 1300 and 1400 UTC (Fig. 3). The first instance, detected between 1311 and 1315 UTC, and peaking at 1314 UTC, was located above Sardinia. The UHSAS-A and PCASP data revealed a huge

increase of around 100 particles per cubic centimeter (particles cm⁻³) in the 0.1–0.2- μ m size range, and 400 particles cm⁻³ in the 1.1–3.1- μ m size range. The rapid aerosol burden increase (two tiny spikes and one large peak) was correlated with increases in CO from ~100 to ~270 ppbv, O₃ from ~35 to ~70 ppbv, and CH₄ from ~1,900 to ~1,935 ppbv, while relative humidity dropped from 55% to 35%. During this episode, the aircraft flew through a thin, dark layer, typical of carbonaceous particles, located at an altitude of approximately 9 km (not shown). The aerosol measurements were delayed by 12 s compared to all the other measurements because of delays in the data analysis of outdoor (aerosols) versus indoor (all other species) records. The aerosol measurements presented in Fig. 3 take into account this adjustment.

The second episode occurred between 1351 and 1359 UTC, peaking at 1354 UTC. It was detected farther west, above Minorca, by UHSAS-A and PCASP and showed an elevated aerosol burden of ~450 particles cm⁻³ in the 0.1–0.2- μ m size range and ~200 particles cm⁻³ in the 1.1–3.1- μ m size range. This second episode was accompanied by a very weak increase in O₃ (~6 ppbv), CO (~10 ppbv), and CH₄ (~10 ppbv) but showed a significant increase in relative humidity from 80% to 100%, detected at 1354 UTC.

To assess the origin and nature of the aerosols measured during these two episodes, HYSPLIT was used to calculate 20-day back trajectories from the location, time, and altitude (~300 hPa) of

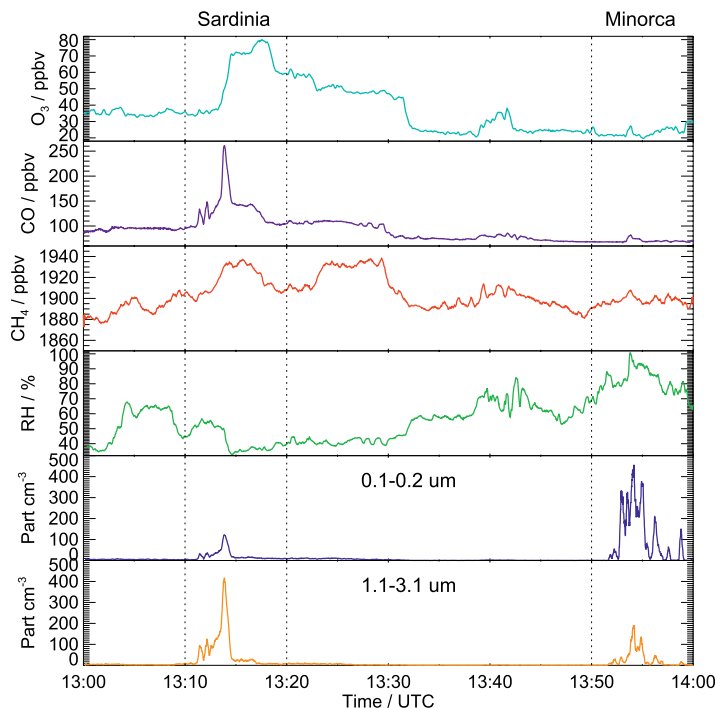
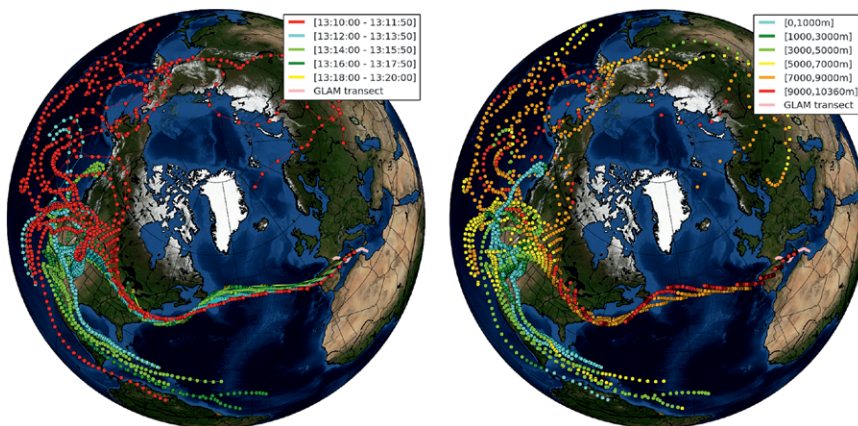


FIG. 3. (top to bottom) Time series of different compounds measured during flight 8 (between 1300 and 1400 UTC 10 Aug 2014) at an altitude of 9.7-km altitude (from east of Sardinia to west of Minorca): O₃ (light blue), CO (purple), CH₄ (red), and relative humidity (RH; green). Aerosols (particles cm⁻³) were measured by the UHSAS-A instrument (blue) in the 0.1–0.2- μ m size range and the PCASP instrument (orange) in the 1.1–3.1- μ m size range. Note that CO and RH represent raw data, while O₃, CH₄, and aerosols have been averaged using a 12-s running mean. Vertical dotted lines between 1310 and 1320 UTC and 1350 and 1400 UTC show the times during which the aircraft was above Sardinia and Minorca, respectively.

FIG. 4. The 20-day back trajectories initiated above Sardinia (1310–1320 UTC) at the altitude of the aircraft (~300 hPa), calculated by HYSPLIT every 6 h (one filled circle). (left) The trajectories are separated into five sets of 2-min intervals elapsing between 1310 and 1320 UTC: 1310–1312 (red), 1312–1314 (blue), 1314–1316 (light green), 1316–1318 (dark green), and 1318–1320 UTC (yellow). (right) The trajectories are separated into six sets along the vertical between 0 and 11 km: 0–1 (blue), 1–3 (dark green), 3–5 (light green), 5–7 (yellow), 7–9 (orange), and 9–11 km (red). The GLAM transect is represented by a pink line.



the respective aerosol observations over Sardinia (1310–1320 UTC) and Minorca (1350–1400 UTC). By tracing back trajectories from Sardinia (Fig. 4), it was revealed that the air parcels had originated in the northern territories (Canada) above an altitude of 7 km (1310–1312 UTC) and the United States below 7 km (1310–1320 UTC). Canada’s northern territories and the western United States were regions in which numerous fires had been identified by MODIS over the course of more than 1 month (Fig. 5, top).

According to the Global Fire Emission Database (GFED; www.globalfiredata.org/), 2014 was the most intense year during the period 1997–2014 in terms of annual fire carbon emissions in the North American

boreal region. In 2014, the annual CH₄ emission estimate associated with forest fires was 1.22 Tg CH₄ compared with a 1997–2014 mean of 0.63 Tg CH₄. Annual peat fire emissions for 2014 were estimated to be 0.39 Tg CH₄ compared with a 1997–2014 mean of 0.15 Tg CH₄. It should be noted that the impact of permafrost thaw on CH₄ release may have been underestimated (Lawrence et al. 2015). In North America, pyroconvection processes associated with long-lasting and intense fires could explain the injection of black carbon, carbon monoxide, ozone, and methane into the mid- to upper troposphere and even the lower stratosphere (e.g., Fromm and Servranckx 2003). Smoke plumes of North American origin

have already been observed over Europe and the Mediterranean (Forster et al. 2001; Formenti et al. 2002). They have also been recently analyzed using airborne and spaceborne sensors during the Aerosol Direct Radiative Impact in the Mediterranean (ADRIMED) experimental campaign (Ancellet et al. 2016). Elevated concentrations of CO and black carbon (Fig. 5, bottom left) caused by forest fires were indicated by MOCAGE over North America between 1 and 10 August.

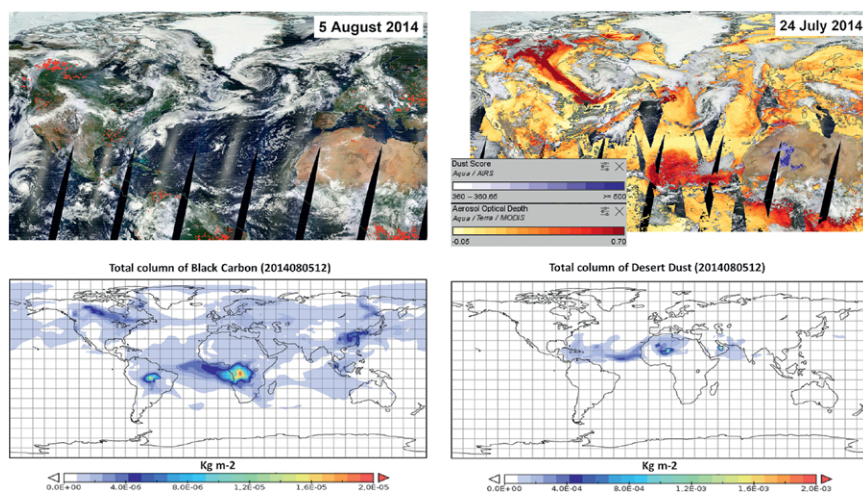


FIG. 5. (top left) MODIS reflectance (true color) and fires/thermal anomalies (red dots) as measured on 5 Aug 2014, showing intense fire events in the northern territories (Canada) and California/Oregon (United States). (top right) Multiple satellite images from AIRS (dust score, purple scale) and MODIS (aerosol optical depth, orange scale) overlaid on the corrected reflectance as measured by MODIS (grayscale) on 24 Jul 2014, showing the dust outflow from Africa and its propagation over the Atlantic Ocean. Dust scores greater than 400 indicate high levels of atmospheric aerosols. The coastlines are shown in dark gray. (bottom) Total column (kg m^{-2}) of (left) black carbon and (right) desert dust as calculated by MOCAGE at 1200 UTC 5 Aug 2014.

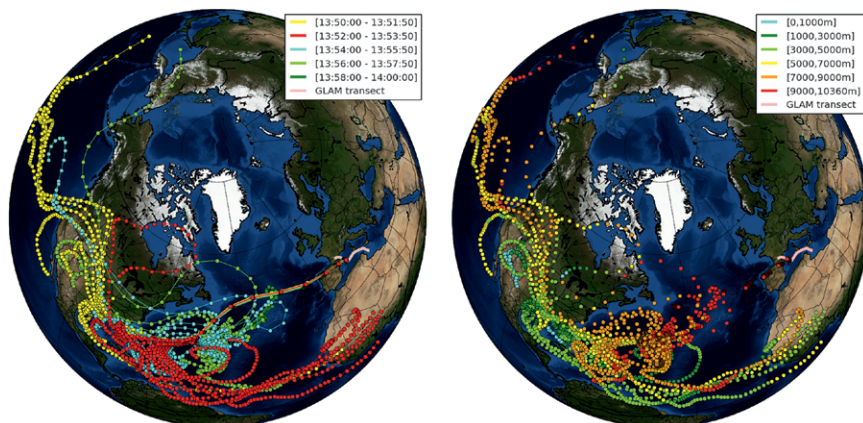


FIG. 6. As in Fig. 4, but initiated above Minorca (1350–1400 UTC). (left) The trajectories are separated into five sets of 2-min intervals elapsing between 1350 and 1400 UTC: 1350–1352 (yellow), 1352–1354 (red), 1354–1356 (blue), 1356–1358 (light green), and 1358–1400 UTC (dark green).

Over Minorca (Fig. 6), the 20-day back trajectory calculation using HYSPLIT revealed that the majority of air parcels can be divided into two main routes: the first originating in West Africa (1352–1354 UTC) within an altitude range of 3–7 km and the second originating in the United States (remaining time periods) below an altitude of 7 km. The two routes converge to a strong depression located in the Atlantic Ocean (35°N, 50°W) and rapidly lift both pollutants and black carbons originating in the United States and

desert dusts originating in the Sahara from the lower-/midtroposphere to the upper troposphere. Indeed, MODIS desert dust images show regular aerosol outbursts (occurring every 2–3 days) traveling from the Sahara Desert to the Atlantic Ocean and toward the Caribbean Sea (Fig. 5, top right). This is consistent with the satellite climatology on African dust transport to the Atlantic (Moulin et al. 1997). It is worth mentioning that the HYSPLIT 20-day back trajectory calculations initiated above Sardinia and Minorca were consistent with the trajectories calculated using FLEXPART and BADC (not shown).

Measurements taken of aerosols using the spaceborne lidar Cloud–Aerosol Lidar with Orthogonal Polarization (CALIOP) on board the CALIPSO platform (Fig. 7) found, for example, the vertical structure of two aerosol subtypes during one nighttime orbit above the Atlantic Ocean at 0550 UTC 5 August 2014: 1) smoke over the northern part of the orbit (latitudes 50°–57°N, North Atlantic) at altitudes of between 2 and 7 km and 2) desert dust over the southern part of the orbit (latitudes

20°–25°N, Caribbean Sea/Bahamas) at altitudes of between 0 and 4 km, which would support our findings over Minorca.

Whichever routes explored from Sardinia or Minorca, at some stage the back trajectories encountered traces of stratiform and convective precipitation when ARPEGE meteorological analyses (not shown) were used. The impact of this is more significant over Minorca than Sardinia since trajectories initiated above Minorca reach lower latitudes than trajectories initiated above Sardinia. It has been established that once an air parcel encounters convective precipitation, it loses memory of its source region (Anderson et al. 2016). Nevertheless, using

the FLEXPART model, which includes washout processes (wet and dry depositions), it was possible to discern two routes arriving at Minorca (from West Africa and the United States) and one main route arriving at Sardinia from the United States/Canada (not shown). These findings are consistent with the outputs from the HYSPLIT model (see above). Furthermore, it has been confirmed that aerosols over Sardinia have their origins in biomass burning, while aerosols over Minorca come from desert dust. Finally, taking into account the ARPEGE analyses along the back trajectories, which include washout processes, we found that relative humidity was ~40%–50% above Sardinia and ~95%–100% above Minorca. These results are entirely consistent with the in situ airborne measurements taken during the GLAM campaign, which found relative humidity to be 35%–50% above Sardinia and 85%–100% above Minorca (see Fig. 3).

EASTERN MEDITERRANEAN. We will now turn to discussing the results from the GLAM vertical profiles measured around Cyprus on 8 August. The three O₃ profiles—P5 ascent, P5 descent, and P6 descent—are presented in Fig. 8 (left), which displays pressure data alongside vertical profiles from the MOCAGE model, the CAMS/C-IFS analyses at 1800 UTC, and

the daily averaged OMI/MLS O₃ measurements for 8 August. It is worth noting the consistency of the O₃ profile shapes from OMI/MLS, CAMS/C-IFS, MOCAGE, and GLAM, which show values of 52 ± 10 ppbv between the surface and 950 hPa (i.e., less than ~500 m), a first maximum of ~100 ppbv at 750–650 hPa (2.5–4.0 km), and a second maximum of 80–90 ppbv at 340–410 hPa (7.0–9.0 km). It is also worth noting the increasing variability with altitude between the observational datasets, the model outputs, and the analyses. Moreover, in the uppermost troposphere, the GLAM O₃ mixing ratio decreases with altitude from 40 ppbv above 300 hPa to a few parts per billion by volume at 200 hPa. Model outputs and satellite data indicate relatively low but rather constant values (45–75 ppbv) in this altitude range (Fig. 8). Upper-tropospheric O₃ minima, although infrequent, have already been reported in previous studies (e.g., Kley et al. 1996; Lawrence et al. 1999; Asman et al. 2003; Sahu et al. 2006). These studies pointed to, first, a probable (sub)tropical marine boundary layer origin and, second, the fact that the O₃ concentration remained constant during transport from the boundary layer to the upper troposphere. If we now consider the full range of constituents measured by the GLAM campaign, namely, H₂O,

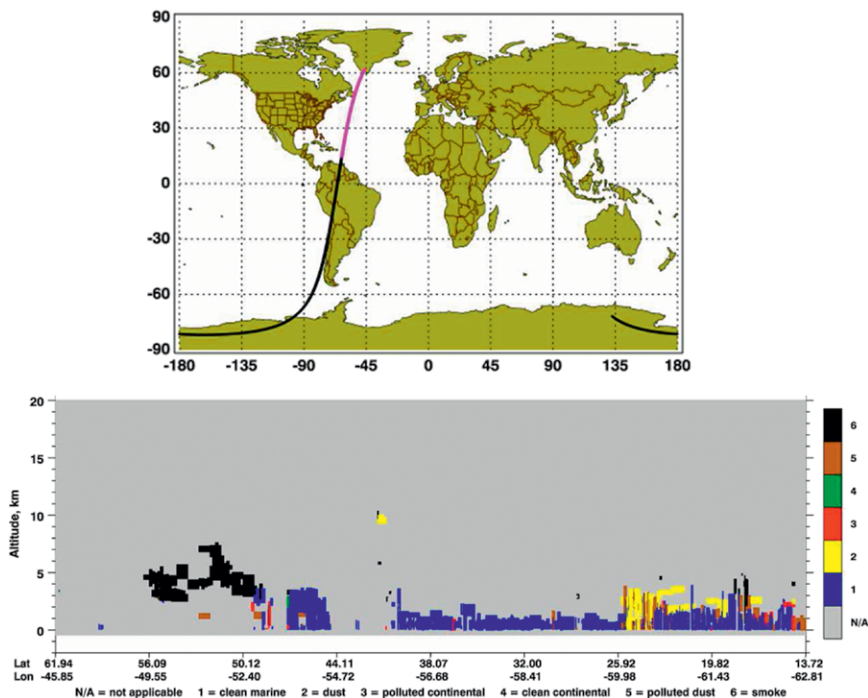


FIG. 7. (top) Nighttime orbit (pink portion of the orbit track) of the CALIPSO platform at 0550 UTC 5 Aug. (bottom) Vertical distribution of aerosol subtypes measured along the same orbit showing smoke (black), polluted dust (brown), dust (yellow), clean marine (blue), and polluted continental (red).

O₃, CO, CH₄, and CO₂ (Fig. 8, right), the P5 profile produced on 8 August revealed a thick layer (labeled [I] in Fig. 8, right) between an altitude of 12.1 and 12.8 km (192–213 hPa) with a signature of low O₃, CO, and CH₄ and high CO₂ and H₂O.

To ascertain the origin of the 12.1–12.8-km-thick layer detected during the GLAM campaign, we calculated 10-day back trajectories for air masses at 180, 185, 190, and 195 hPa at 1800 UTC 8 August, which corresponded in terms of time and location with the vertical profiling performed during flight P5. Results are displayed on a latitude–longitude map (Fig. 9, top)

and along the vertical (Fig. 9, bottom). All the 10-day back trajectories indicate that the air masses originated above the Arabian Sea below 750 hPa and, for two of them, below 900 hPa within the maritime atmospheric boundary layer. Following the route of the back trajectories, the MOCAGE model indicated particularly low O₃ concentrations (less than 20 ppbv) in the maritime boundary layer over the Arabian Sea, which is consistent with the surface O₃ analyses provided by the CAMS/C-IFS project (Fig. 9, top). The O₃-depleted upper-tropospheric air over the eastern Mediterranean appears to be caused by long-range transport of the

clean maritime atmospheric boundary layer above the Arabian Sea as well as a lack of O₃ photochemistry during transport. These O₃-depleted air masses moved from the Arabian Sea to the Indian subcontinent above the planetary boundary layer (800–600 hPa). Once inside the Asian monsoon system above Bangladesh (Fig. 9, bottom), they were lifted within less than 24 h to the upper troposphere (~150 hPa) and redistributed toward the eastern Mediterranean basin over the course of a few days via the Asian monsoon anticyclone. All of this is consistent with the general processes described in Ricaud et al. (2014) and would explain the anomalously low O₃ values in the upper troposphere above Larnaca. It is worth noting that all air masses originating in the Arabian Sea's maritime boundary layer show a minimum in CH₄ and CO and a maximum in CO₂ using CAMS/C-IFS and a maximum in H₂O using meteorological analyses (not shown).

East–west variability. The east–west variability of O₃, CO, CH₄, and CO₂ was

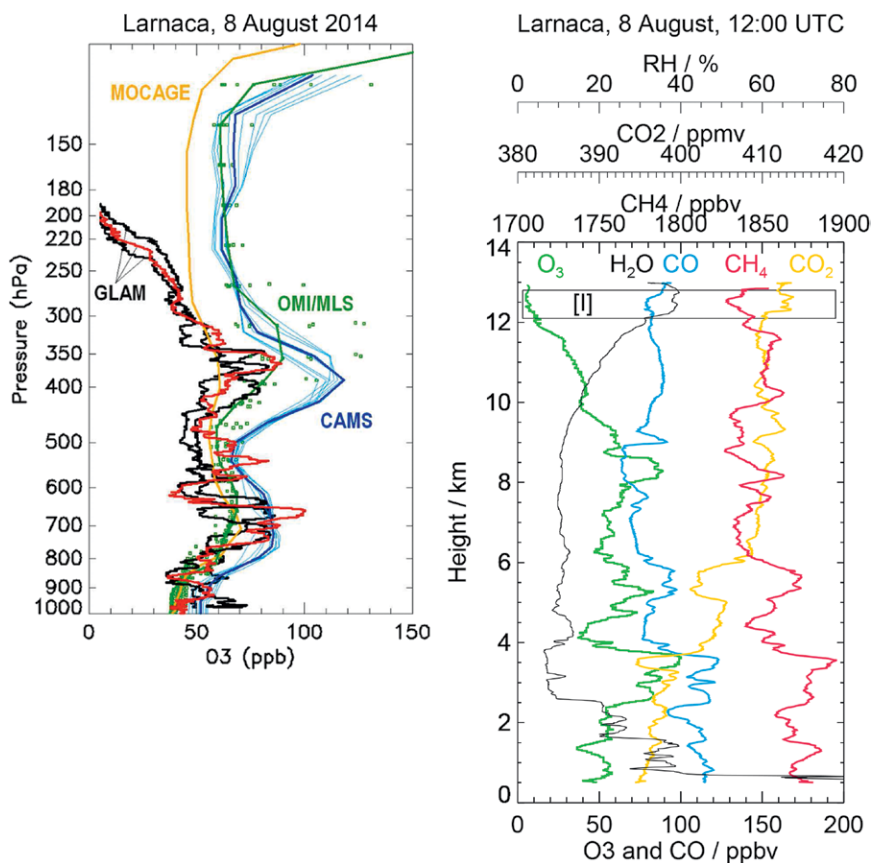


FIG. 8. (left) The O₃ vertical distributions vs pressure measured by GLAM on 8 Aug 2014 in the vicinity of Cyprus during the P5 ascent (red) and descent (black) around 1200 UTC, and the P6 descent at ~1800 UTC (black). Overlaid on this are the CAMS/C-IFS model results (blue) at 1800 UTC, the OMI/MLS assimilated daily products (green), and the MOCAGE model results (orange) at 1800 UTC. Note that the green line represents the daily averaged OMI/MLS profile at 34°N, 32.5°E, while the green stars highlight the variability within 34°N ± 2°, 32.5°E ± 2.5°. Similarly, the CAMS/C-IFS thick blue line represents the profile at 34.5°N, 32.25°E, while the thin blue lines highlight the variability within 34.5°N ± 0.75°, 32.25°E ± 0.75°, all of them modeled at 1800 UTC. (right) The O₃ (green), CO (blue), CH₄ (red), CO₂ (orange), and RH (black) vertical profiles as measured during the P5 ascent. The vertical layer labeled “[I]” represents a domain impacted by the lowermost troposphere of the Arabian Sea (see text and Fig. 9). Note that all the measurements, analyses, and model outputs shown have been averaged using a 10-s running mean.

investigated using GLAM in situ measurements and the CAMS/C-IFS analyses along the two horizontal transects between Minorca and Larnaca at an altitude of 5.4 km and Larnaca and Minorca at an altitude of 9.7 km. Figure 10, for example, illustrates the west-to-east variability of the four constituents at an altitude of 5.4 km along the three F2–4 flight tracks from Minorca to Larnaca, with GLAM and CAMS in collocation. It should be noted that the GLAM data have been averaged using a 20-s running mean. The CAMS/C-IFS analyses used in Fig. 10 are the analyses run at 1200 UTC on the relevant day as well as those run at 0600 UTC for flight F3 on 7 August, all of which used a 0.7° horizontal resolution. For the sake of clarity, in Fig. 10, the CAMS/C-IFS O₃ analyses have been debiased against the GLAM data by -30 ppbv. The means over the three flights in the GLAM measurements and in the CAMS/C-IFS analyses are calculated to be 50.7 and 81.9 ppbv for O₃; 94.9 and 84.8 ppbv for CO; 1,860.7 and 1,864.8 ppbv for CH₄; and 399.1 and 394.2 ppmv for CO₂. The associated standard deviations σ in the GLAM measurements and in the CAMS/C-IFS analyses are 15.0 and 16.3 ppbv for O₃; 20.8 and 8.9 ppbv for CO; 18.8 and 13.5 ppbv for CH₄; and 3.2 and 2.5 ppmv for CO₂. On average, there is a systematic difference between GLAM measurements and CAMS/C-IFS analyses as regards O₃ and CO₂, this being around -30 ppbv for the former, and +5 ppmv for the latter, greater than the intrinsic variability σ of the datasets. However, this difference is insignificant in the case of CO₂, since the overall uncertainty for GLAM is 8 ppmv. Consequently, the variability σ within the GLAM measurements and the CAMS/C-IFS analyses is very consistent, although GLAM CO variability is about twice as great as that of CAMS/C-IFS. It is important to note that the systematic negative difference of -30 ppbv between GLAM O₃ observations and CAMS/C-IFS O₃ analyses at an altitude of 5.4 km is consistent with the negative difference between OMI/MLS O₃ analyses and MOCAGE O₃ outputs and that of CAMS/C-IFS at 500 hPa, which is approximately 10–15 ppbv (Fig. 8).

In general, the fine structures in the longitudinal variability of the four species measured during the campaign GLAM are well captured by the CAMS/C-IFS analyses. For instance, on flight F2 at 1200 UTC, the net increase in O₃, CO, and CH₄ at 9°E longitude is present in the GLAM measurements and in the CAMS/C-IFS analyses, although this increase was about 2 times as large in the GLAM CH₄ data and 3 times as large for the CO data. The significant difference in terms of the horizontal resolution used by

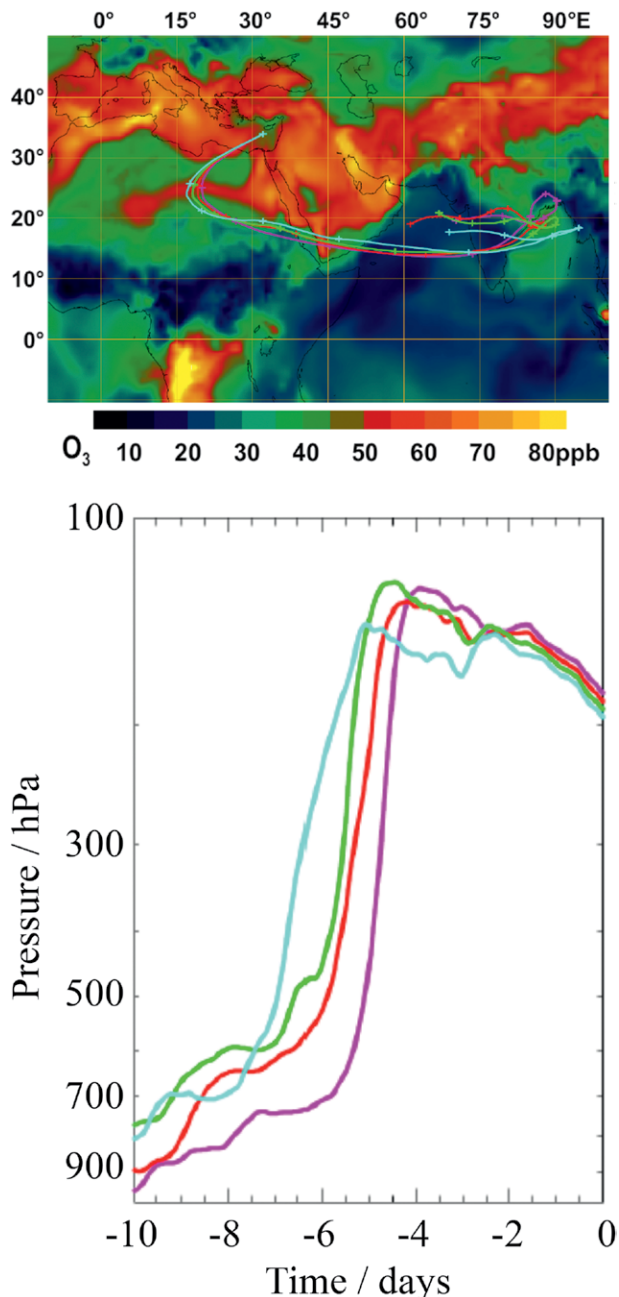


Fig. 9. (top) The 10-day back trajectories for air parcels located at 33.94°N, 32.05°E at 1800 UTC 8 Aug at 180 (pink line), 185 (red line), 190 (green line), and 195 (blue line) hPa. The trajectories are superimposed on the CAMS/C-IFS map for O₃ at 1,000 hPa at 1800 UTC 29 Jul 2014. **(bottom)** Vertical position (hPa) for the same 10-day back trajectories as provided in the top panel.

CAMS/C-IFS (70 km) and GLAM (200–400 m) could explain the disparity in the number of fine structures in the datasets. The west–east transect during F2 shows a net negative tendency in the GLAM CO₂ observations and in the CAMS/C-IFS CO₂ analyses. On

F3, GLAM measurements were taken at 0830 UTC. The importance of time coincidence when comparing CAMS/C-IFS analyses either at 0600 or 1200 UTC with the GLAM data are plain, since field structures can be either similar or delayed. At 0600 UTC, the CAMS/C-IFS analyses show a local maximum in O_3 at around $17^\circ E$ longitude in accordance with the GLAM data, but no maximum in O_3 , CO , and CH_4 at $21^\circ E$ longitude. Conversely, at 1200 UTC, the CAMS/C-IFS analyses show a local minimum in O_3 at around $17^\circ E$ longitude in contradiction with the GLAM data but a maximum of O_3 , CO , and CH_4 at $21^\circ E$ longitude in complete accordance with GLAM data. Both analyses tend to show a negative west–east tendency for CO_2 from 12° to $23^\circ E$ as is supported by the GLAM data. Along flight F4 at 1300 UTC, the GLAM measurements and CAMS/C-IFS analyses for O_3 and CO fields at 1200 UTC agree, while the CH_4 and CO_2 fields differ. Finally, the Global Forecast System (GFS) of

NCEP indicated that the maxima of pollutants (O_3 and CO) and greenhouse gases (i.e., CH_4) observed by GLAM and analyzed in CAMS/C-IFS over Lampedusa on 6 August and Heraklion on 7 August were predominantly driven by the westerlies and the position of the low pressure system over Slovenia, which moved eastward to the Aegean Sea (not shown). The west–east gradient at an altitude of 5.4 km is essentially produced by regional atmospheric conditions but is also affected by the chemistry on a global scale because of the long-range transport of pollutants and greenhouse gases. This study on the tropospheric chemistry of different lifetime chemical species underlines how important a multiscale geographical and temporal approach is if we are to understand the origin of the anomalies and processes involved.

Comparisons with measurements obtained from surface stations. To further assess the quality of

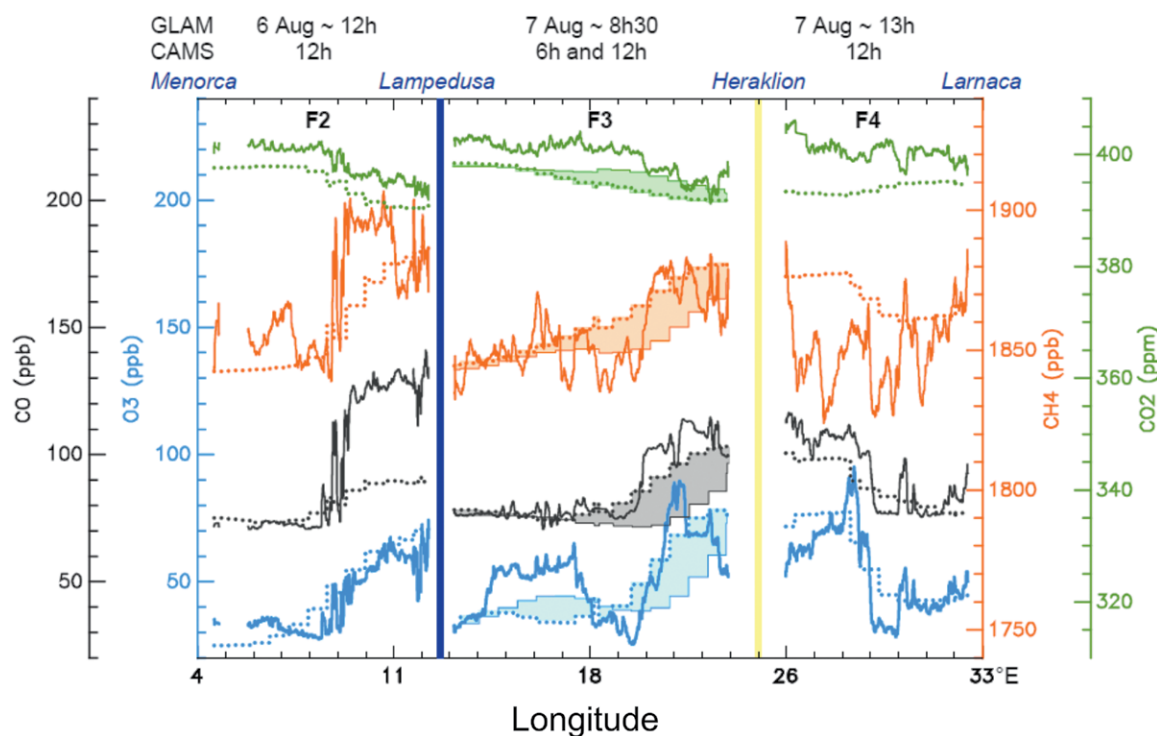


FIG. 10. West–east gradient: comparisons between GLAM (thick solid line) and CAMS/C-IFS (dotted line) analyses for the three transects (flights F2–F4) for O_3 (blue), CO (black), CH_4 (orange), and CO_2 (green). The flights followed a route from Minorca (at 1200 UTC 6 Aug) to Larnaca (at 1300 UTC 7 Aug) via Lampedusa and Heraklion and flew at an altitude of 5 km. Note that CAMS/C-IFS analyses for O_3 have been debiased by -30 ppbv. CAMS/C-IFS analyses were carried out at 1200 UTC, except during flight F3 (middle panel) between Lampedusa and Heraklion at 0830 UTC 7 Aug, for which CAMS/C-IFS analyses are also shown at 0600 UTC (thin solid line). The domain between 0600 and 1200 UTC has been shaded. The thick vertical dark blue line represents a 12-h nighttime stopover in Lampedusa between 6 and 7 Aug (in between F2 and F3), while the yellow vertical line represents a 2-h stopover in Heraklion around 1100 UTC 7 Aug in between F3 and F4. Note that all the GLAM data shown have been averaged using a 20-s running mean.

the GLAM measurements, we also used coincident measurements obtained from surface stations during the campaign. The time evolution data for O_3 , CO , CH_4 , CO_2 , and aerosols provided by these surface stations (Table 2) has been compared with GLAM airborne measurements taken over Lampedusa (Italy), Finokalia (Greece), and Cyprus. For the purposes of this study, we have only provided the aerosol vertical distributions investigated above Lampedusa and Limassol, comparing the GLAM profiles from the PCASP and UHSAS-A instruments, as well as the ground-based lidar instruments, with the outputs from the ALADIN-Climate and MOCAGE models. Figure 11 shows the number of aerosol particles integrated within several size ranges (137–234 nm for UHSAS-A and 105–550 nm for PCASP) along the vertical from 1310 to 1350 UTC (descending phase), derived from the GLAM P2 profile produced on 6 August at Lampedusa, along with the vertical distribution of the aerosol backscattering coefficient measured between 1310 and 1350 UTC

by the backscatter lidar installed on Lampedusa. The aerosol profile at Lampedusa is obtained with a fixed value of the extinction-to-backscatter ratio of 30 sr; this value is the most probable for desert dust found at Lampedusa [see Di Iorio et al. (2009) for further details on the backscatter lidar]. In the same figure, we have also provided the vertical distribution of total aerosols (sea salt, dust, organic aerosols, and black carbon) from the two models at Lampedusa at 1200 UTC 6 August. Although the GLAM profiles are obviously noisier than the lidar 30-m vertical resolution profiles, they all show 1) a maximum centered

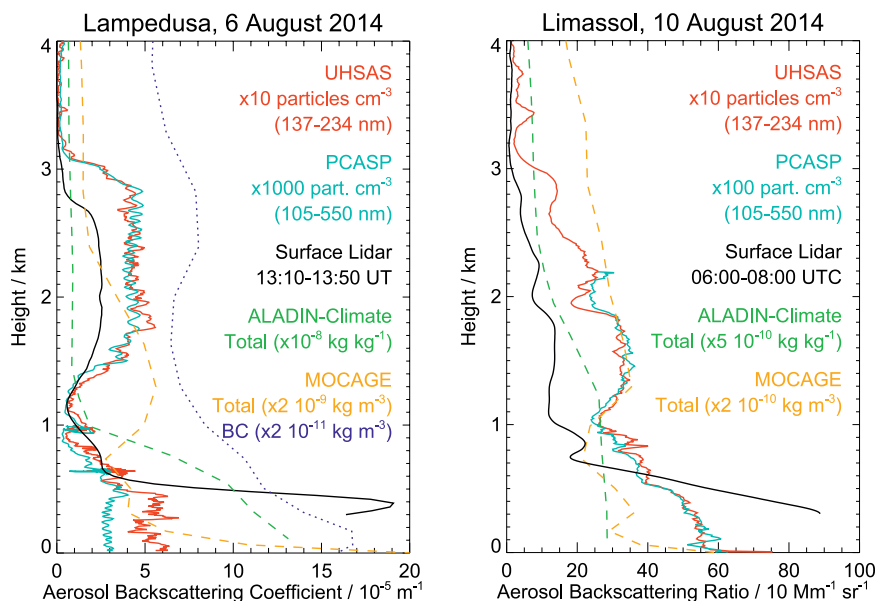


FIG. 11. (left) Vertical distributions of aerosol backscattering coefficient ($\times 10^{-5} \text{ m}^{-1}$) measured between 1310 and 1350 UTC 6 Aug by the backscatter lidar instrument at Lampedusa (black line) alongside the number of particles cm^{-3} measured by UHSAS-A ($\times 10$) in the 137–234-nm size range (red) and PCASP ($\times 1,000$) in the 105–550-nm size range (light blue) in the vicinity of Lampedusa (mainly above the Mediterranean Sea) while collecting the P2 vertical profile. Also included are vertical distributions of the total aerosol (sea salt, dust, organic aerosol, and black carbon) mixing ratios ($\times 10^{-8} \text{ kg kg}^{-1}$) calculated by ALADIN-Climate (green dashed line) and concentrations ($\times 2 \times 10^{-9} \text{ kg m}^{-3}$) calculated by MOCAGE (orange dashed line), with an emphasis on BC concentrations ($\times 2 \times 10^{-11} \text{ kg m}^{-3}$) calculated by MOCAGE (dotted dark blue) over Lampedusa at 1200 UTC 6 Aug. (right) Vertical distributions of aerosol backscattering ratio ($\times 10 \text{ Mm}^{-1} \text{ sr}^{-1}$) measured between 0600 and 0800 UTC 10 Aug by the Raman-polarization lidar system at Limassol (black line), alongside the number of particles cm^{-3} measured by UHSAS-A ($\times 10$) in the 137–234-nm size range (red) and by PCASP ($\times 100$) in the 105–550-nm size range (light blue) in the vicinity of Limassol, Crete (mainly above the Mediterranean Sea), when taking off on flight F7 at 0704 UTC. Also shown are the vertical distributions of total aerosol (sea salt, dust, organic aerosol, and black carbon) mixing ratios ($5 \times 10^{-10} \text{ kg kg}^{-1}$) calculated by ALADIN-Climate (dashed green line) and concentrations ($\times 2 \times 10^{-10} \text{ kg m}^{-3}$) calculated by MOCAGE (dashed orange) over Limassol at 0600 UTC 10 Aug. Note that the PCASP and UHSAS-A measurements have been averaged using a 5-s running mean.

at $\sim 400 \text{ m}$ in the lidar data and $\sim 400\text{--}500 \text{ m}$ in the GLAM data, representing the boundary layer and 2) a wide secondary maximum at altitudes of between 1 and 3 km, representing the free troposphere. It is worthwhile mentioning that, because of instrumental limitations, the lidar signal below 300-m altitude cannot be used to retrieve a trustworthy backscattering profile. Although the peak at 400 m is a reliable feature in the aerosol profile, we cannot exclude that other layers with elevated backscattering are present below 300 m. The two models show a net maximum below 800–1,000 m, caused mainly

by sea salt and organic aerosols, which is consistent with the GLAM measurements. Above an altitude of 1 km, the two models differ: the vertical distribution of total aerosols produced by ALADIN-Climate is constant, while the MOCAGE distribution shows a pronounced maximum around 1.3 km, mainly caused by dust. At altitudes between 2 and 3 km, MOCAGE indicated a local maximum for black carbon concentrations. This is consistent with GLAM measurements, which suggested a maximum for particles or scattering coefficients at altitudes between 1 and 3 km. The 10-day back trajectories were calculated from Lampedusa at 1300 UTC 6 August (not shown). At 400 m (local aerosol maximum), air masses all originated from the west in the polluted European planetary boundary layer. Between 800 and 1,600 m (MOCAGE local dust maximum), the majority of air masses originated from the west of the Atlantic Ocean around 30°N, where it has been previously demonstrated that desert dust from the Sahara is regularly deposited at this time of year. This would explain why the ALADIN-Climate model was unable to calculate this maximum, since the sources were located outside of its study domain. At altitudes of between 2 and 3 km (MOCAGE local black carbon maximum), the majority of air masses originated from North America at latitudes greater than 45°N, where it has been previously demonstrated that fires were present at this time of year. This would again explain the absence of black carbons in this layer indicated by the ALADIN-Climate model.

The vertical distribution of aerosols was also investigated based on the GLAM measurements gathered during flight F7, which took off from Larnaca on 10 August. The PCASP and UHSAS-A instruments and the Raman polarization lidar system of Cyprus University of Technology installed at Limassol (10 m MSL) were used as well as the outputs from the ALADIN-Climate and MOCAGE models. The number of particles integrated within the same size ranges as described above for Lampedusa along the vertical at 0704 UTC are shown alongside the vertical distribution of the aerosol backscattering coefficient measured by the lidar system and averaged between 0600 and 0800 UTC (Fig. 11, right). The full overlap of the laser beam with the receiver field of view of the 20-cm Cassegrain telescope is obtained at heights around 300 m MSL. The overlap characteristics were checked by Raman lidar observations under clear-sky conditions at Limassol and the particle optical depth measured with a collocated sun photometer have been used as a constraint on the retrievals of the backscatter coefficient [see Mamouri et al. (2013),

Nisantzi et al. (2015), and Mamouri and Ansmann (2014) for further details on the lidar system]. In the same figure, we have also provided the vertical distribution of total aerosols (sea salt, dust, organic aerosol, and black carbon) obtained from the two models run at Limassol at 0600 UTC 10 August. All the measurements and model outputs except for those of ALADIN-Climate show a maximum aerosol loading in the boundary layer (300–1,000 m) and a secondary maximum at altitudes between 1 and 2 km. By comparison, ALADIN-Climate only indicated a local maximum in the lower troposphere (0–1 km). The 10-day back trajectories were calculated from Limassol at 0700 UTC 10 August (not shown). At an altitude of 400 m (first aerosol maximum), air masses mainly originated from the north in the polluted European planetary boundary layer and were composed of sea salt and organic aerosols. Between 1,000 and 2,000 m (second aerosol maximum), air masses originated from the north in the lower troposphere above Europe, at altitudes between 1,000 and 3,000 m, and were mainly composed of dust. Above an altitude of 3 km, air masses originated from the west in the polluted midtroposphere above the North American continent (4,500–6,000 m) and were affected by forest fire emissions as has been previously discussed.

FINAL COMMENTS. To investigate the summertime variability of different chemical constituents and aerosols between the west (~3°E) and east (~35°E) of the Mediterranean basin, as well as the impact of long-range transport on this variability, an airborne campaign was set up in August 2014 as part of the Chemistry–Aerosol Mediterranean Experiment (ChArMEx) initiative in the framework of the Mediterranean Integrated Studies at Regional And Local Scales (MISTRALS) program. The Gradient in Longitude of Atmospheric Constituents above the Mediterranean Basin (GLAM) airborne campaign took place from 6 to 10 August 2014 and followed a route from Toulouse (France) to Larnaca (Cyprus) via Minorca (Spain), Lampedusa (Italy), and Heraklion (Crete). The outbound flight altitude was 5.4 km MSL, while on the return flight the altitude was 9.7 km MSL. Vertical profiles were also collected between the surface and approximately 12 km MSL around the landing sites. Aerosols, winds, radiation, humidity, and chemical compounds (O_3 , CO , CH_4 , and CO_2) were measured in situ by basic instruments and an infrared laser spectrometer (SPIRIT instrument) aboard the SAFIRE F-20 aircraft. The CAMS/C-IFS forecasts and analyses provided by

ECMWF, along with satellite and surface measurements and model outputs, and back and forward trajectory calculations helped in the interpretation of the measurements obtained during the GLAM campaign. Of all the results yielded over the course of the eight flights, the variability of pollutants, greenhouse gases, and aerosols along the vertical and the horizontal between the boundary layer and the upper troposphere, and the west and east of the Mediterranean basin, tend to show the impact of intercontinental transport. Different corridors were explored from North America, West Africa, Asia, and the Arabian Sea. Models tend to reproduce the variability observed in the GLAM in situ measurements but with fewer structures and with some biases. These key results will be more thoroughly examined, along with several new processes (such as subsidence, stratosphere-to-troposphere transport, and surface measurements) in forthcoming papers (e.g., Brocchi et al. 2017, manuscript submitted to *Atmos. Chem. Phys. Discuss.*). The success of the GLAM campaign and the results obtained, which demonstrate the strong link in summer between the eastern Mediterranean basin and Asia, particularly the Arabian Sea/Peninsula and the Indian subcontinent, emphasize the need for a new airborne campaign to be conducted between these two regions as part of the ChArMEX project.

ACKNOWLEDGMENTS. We thank the following institutes and programs for funding our study: Centre National de la Recherche Scientifique-Institut National des Sciences de l'Univers (CNRS-INSU); Météo-France; Agence de l'Environnement et de la Maîtrise de l'Energie (ADEME) through the Mediterranean Integrated Studies at Regional And Local Scales (MISTRALS)/Chemistry-Aerosol Mediterranean Experiment (ChArMEX) program; Météo-France and Airbus Space and Defense for funding Y. Kangah's PhD thesis; Labex VOLTAIRE (ANR-10-LABX-100-01) for funding V. Brocchi's Ph.D. thesis; Météo-France and the Région Midi-Pyrénées for funding N. Jaidan's Ph.D. thesis; and NextData MIUR Project for funding surface O₃ measurements at Lampedusa. SAFIRE is a joint facility provided by CNRS, Météo-France, and CNES dedicated to flying research aircraft. We thank Dr. C. Delire and Dr. C. Carcaillet for their helpful discussions on methane emissions induced by fire and permafrost. Thanks are also due to the British Atmospheric Data Centre, part of the Natural Environment Research Council's (NERC) National Centre for Atmospheric Science (NCAS), for calculating trajectories and providing access to European Centre for Medium-Range Weather Forecasts (ECMWF) data; the Global Modeling and

Assimilation Office (GMAO) at NASA's Goddard Space Flight Center for the OMI and MLS analysis; and NASA's EOSDIS Worldview facilities for their MODIS and AIRS data. Finally, we thank the two anonymous reviewers for their fruitful comments.

REFERENCES

- Agustí-Panareda, A., and Coauthors, 2014: Forecasting global atmospheric CO₂. *Atmos. Chem. Phys.*, **14**, 11 959–11 983, <https://doi.org/10.5194/acp-14-11959-2014>.
- Ancellet, G., and Coauthors, 2016: Long-range transport and mixing of aerosol sources during the 2013 North American biomass burning episode: Analysis of multiple lidar observations in the western Mediterranean Basin. *Atmos. Chem. Phys.*, **16**, 4725–4742, <https://doi.org/10.5194/acp-16-4725-2016>.
- Anderson, D. C., and Coauthors, 2016: A pervasive role for biomass burning in tropical high ozone/low water structures. *Nat. Commun.*, **7**, 10267, <https://doi.org/10.1038/ncomms10267>.
- Asman, W. A. H., M. G. Lawrence, C. A. M. Brenninkmeijer, P. J. Crutzen, J. W. M. Cuijpers, and P. Nédélec, 2003: Rarity of upper-tropospheric low O₃ mixing ratio events during MOZAIC flights. *Atmos. Chem. Phys.*, **3**, 1541–1549, <https://doi.org/10.5194/acp-3-1541-2003>.
- Benedetti, A., and Coauthors, 2009: Aerosol analysis and forecast in the ECMWF Integrated Forecast System: 2. Data assimilation. *J. Geophys. Res.*, **114**, D13205, <https://doi.org/10.1029/2008JD011115>.
- , J. W. Kaiser, and J.-J. Morcrette, 2011: Aerosols [in “State of the Climate in 2010”]. *Bull. Amer. Meteor. Soc.*, **92**, S65–S67, <https://doi.org/10.1175/1520-0477-92.6.S1>.
- Christoudias, T., A. Pozzer, and J. Lelieveld, 2012: Influence of the North Atlantic Oscillation on air pollution transport. *Atmos. Chem. Phys.*, **12**, 869–877, <https://doi.org/10.5194/acp-12-869-2012>.
- Courtier, P., C. Freydier, J. F. Geleyn, F. Rabier, and M. Rochas, 1991: The ARPEGE project at METEO-FRANCE. *Proc. ECMWF Workshop Numerical Methods in Atmospheric Modelling*, Shinfield Park, Reading, United Kingdom, ECMWF, 193–231.
- Cristofanelli, P., and Coauthors, 2013: Influence of biomass burning and anthropogenic emissions on ozone, carbon monoxide and black carbon at the Mt. Cimone GAW-WMO global station (Italy, 2165 m asl). *Atmos. Chem. Phys.*, **13**, 15–30, <https://doi.org/10.5194/acp-13-15-2013>.
- Dayan, U., P. Ricaud, R. Zbinden, and F. Dulac, 2017: Atmospheric pollution over the eastern

- Mediterranean during summer – a review. *Atmos. Chem. Phys.*, **17**, 13 233–13 263, <https://doi.org/10.5194/acp-17-13233-2017>.
- Dentener, F., D. Stevenson, J. Cofala, R. Mechler, M. Amann, P. Bergamaschi, F. Raes, and R. Derwent, 2005: The impact of air pollutant and methane emission controls on tropospheric ozone and radiative forcing: CTM calculations for the period 1990–2030. *Atmos. Chem. Phys.*, **5**, 1731–1755, <https://doi.org/10.5194/acp-5-1731-2005>.
- Di Iorio, T., A. di Sarra, D. M. Sferlazzo, M. Cacciani, D. Meloni, F. Monteleone, D. Fuà, and G. Fiocco, 2009: Seasonal evolution of the tropospheric aerosol vertical profile in the central Mediterranean and role of desert dust. *J. Geophys. Res.*, **114**, D02201, <https://doi.org/10.1029/2008JD010593>.
- Formenti, P., and Coauthors, 2002: STAAARTE-MED 1998 summer airborne measurements over the Aegean Sea. 1. Aerosol particles and trace gases. *J. Geophys. Res.*, **107**, 4450, <https://doi.org/10.1029/2001JD001337>.
- Forster, C., and Coauthors, 2001: Transport of boreal forest fire from Canada to Europe. *J. Geophys. Res.*, **106**, 22 887–22 906, <https://doi.org/10.1029/2001JD900115>.
- Fromm, M. D., and R. Servranckx, 2003: Transport of forest fire smoke above the tropopause by supercell convection. *Geophys. Res. Lett.*, **30**, 1542, <https://doi.org/10.1029/2002GL016820>.
- Giorgi, F., and P. Lionello, 2008: Climate change projections for the Mediterranean region. *Global Planet. Change*, **63**, 90–104, <https://doi.org/10.1016/j.gloplacha.2007.09.005>.
- Guenther, A., and Coauthors, 1995: A global model of natural volatile organic compound emissions. *J. Geophys. Res.*, **100**, 8873–8892, <https://doi.org/10.1029/94JD02950>.
- Guimbaud, C., and Coauthors, 2011: A portable infrared laser spectrometer for flux measurements of trace gases at the geosphere–atmosphere interface. *Meas. Sci. Technol.*, **22**, 075601, <https://doi.org/10.1088/0957-0233/22/7/075601>.
- Im, U., and M. Kanakidou, 2012: Impacts of east Mediterranean megacity emissions on air quality. *Atmos. Chem. Phys.*, **12**, 6335–6355, <https://doi.org/10.5194/acp-12-6335-2012>.
- Inness, A., and Coauthors, 2015: Data assimilation of satellite-retrieved ozone, carbon monoxide and nitrogen dioxide with ECMWF’s composition-IFS. *Atmos. Chem. Phys.*, **15**, 5275–5303, <https://doi.org/10.5194/acp-15-5275-2015>.
- Kaiser, J. W., and Coauthors, 2012: Biomass burning emissions estimated with a global fire assimilation system based on observed fire radiative power. *Biogeosciences*, **9**, 527–554, <https://doi.org/10.5194/bg-9-527-2012>.
- Kanakidou, M., and Coauthors, 2011: Megacities as hot spots of air pollution in the east Mediterranean. *Atmos. Environ.*, **45**, 1223–1235, <https://doi.org/10.1016/j.atmosenv.2010.11.048>.
- Kangah, Y., and Coauthors, 2017: Summertime mid-to-upper tropospheric nitrous oxide over the Mediterranean as a footprint of Asian emissions. *J. Geophys. Res. Atmos.*, **122**, 4746–4759, <https://doi.org/10.1002/2016JD026119>.
- Kley, D., P. J. Crutzen, H. G. J. Smit, H. Vömel, S. J. Oltmans, H. Grassl, and V. Ramanathan, 1996: Observations of near-zero ozone concentrations over the convective Pacific: Effects on air chemistry. *Science*, **274**, 230–233, <https://doi.org/10.1126/science.274.5285.230>.
- Kuenen, J., H. Denier van der Gon, A. Visschedijk, H. van der Brugh, and R. van Gijlswijk, 2011: MACC European emission inventory for the years 2003–2007. TNO Rep. TNO-060-UT-2011-00588, 49 pp.
- Ladstätter-Weißmayer, A., and Coauthors, 2003: Transport and build-up of tropospheric trace gases during the MINOS campaign: Comparison of GOME, in situ aircraft measurements and MATCH-MPIC-data. *Atmos. Chem. Phys.*, **3**, 1887–1902, <https://doi.org/10.5194/acp-3-1887-2003>.
- Lamarque, J.-F., and Coauthors, 2010: Historical (1850–2000) gridded anthropogenic and biomass burning emissions of reactive gases and aerosols: Methodology and application. *Atmos. Chem. Phys.*, **10**, 7017–7039, <https://doi.org/10.5194/acp-10-7017-2010>.
- Lawrence, D. M., C. D. Koven, S. C. Swenson, W. J. Riley, and A. G. Slater, 2015: Permafrost thaw and resulting soil moisture changes regulate projected high-latitude CO₂ and CH₄ emissions. *Environ. Res. Lett.*, **10**, 094011, <https://doi.org/10.1088/1748-9326/10/9/094011>.
- Lawrence, M. G., P. J. Crutzen, and P. J. Rasch, 1999: Analysis of the CEPEX ozone data using a 3D chemistry-meteorology model. *Quart. J. Roy. Meteor. Soc.*, **125**, 2987–3009, <https://doi.org/10.1002/qj.49712556010>.
- Lelieveld, J., and Coauthors, 2002: Global air pollution crossroads over the Mediterranean. *Science*, **298**, 794–799, <https://doi.org/10.1126/science.1075457>.
- Lionello, P., Ed., 2012: *The Climate of the Mediterranean Region: From the Past to the Future*. Elsevier, 592 pp.
- Liu, J. J., D. B. A. Jones, J. R. Worden, D. Noone, M. Parrington, and J. Kar, 2009: Analysis of the summertime buildup of tropospheric ozone abundances over the Middle East and North Africa as observed by the tropospheric emission spectrometer

- instrument. *J. Geophys. Res.*, **114**, D05304, <https://doi.org/10.1029/2008JD010805>.
- Mamouri, R. E., and A. Ansmann, 2014: Fine and coarse dust separation with polarization lidar. *Atmos. Meas. Tech.*, **7**, 3717–3735, <https://doi.org/10.5194/amt-7-3717-2014>.
- , A. Ansmann, A. Nisantzi, P. Kokkalis, A. Schwarz, and D. Hadjimitsis, 2013: Low Arabian extinction to backscatter ratio. *Geophys. Res. Lett.*, **40**, 4762–4766, <https://doi.org/10.1002/grl.50898>.
- Marenco, A., and Coauthors, 1998: Measurement of ozone and water vapor by Airbus in-service aircraft: The MOZAIC airborne program, an overview. *J. Geophys. Res.*, **103**, 25 631–25 642, <https://doi.org/10.1029/98JD00977>.
- Massart, S., and Coauthors, 2014: Assimilation of atmospheric methane products into the MACC-II system: From SCIAMACHY to TANSO and IASI. *Atmos. Chem. Phys.*, **14**, 6139–6158, <https://doi.org/10.5194/acp-14-6139-2014>.
- , and Coauthors, 2016: Ability of the 4-D-Var analysis of the GOSAT BESD XCO₂ retrievals to characterize atmospheric CO₂ at large and synoptic scales. *Atmos. Chem. Phys.*, **16**, 1653–1671, <https://doi.org/10.5194/acp-16-1653-2016>.
- McQuaid, J., and Coauthors, 2013: In situ trace gas measurements. *Airborne Measurements for Environmental Research: Methods and Instruments*, M. Wendisch and J.-L. Brenguier, Eds., Wiley, 77–155, <https://doi.org/10.1002/9783527653218.ch3>.
- Michou, M., P. Nabat, and D. Saint-Martin, 2015: Development and basic evaluation of a prognostic aerosol scheme (v1) in the CNRM Climate Model CNRM-CM6. *Geosci. Model Dev.*, **8**, 501–531, <https://doi.org/10.5194/gmd-8-501-2015>.
- Morcrette, J.-J., and Coauthors, 2009: Aerosol analysis and forecast in the European Centre for Medium-Range Weather Forecasts integrated forecast system: Forward modeling. *J. Geophys. Res.*, **114**, D06206, <https://doi.org/10.1029/2008JD011235>.
- Moulin, C., C. E. Lambert, F. Dulac, and U. Dayan, 1997: Control of atmospheric export of dust from North Africa by the North Atlantic Oscillation. *Nature*, **387**, 691–694, <https://doi.org/10.1038/42679>.
- Nabat, P., and Coauthors, 2013: A 4-D climatology (1979–2009) of the monthly tropospheric aerosol optical depth distribution over the Mediterranean region from a comparative evaluation and blending of remote sensing and model products. *Atmos. Meas. Tech.*, **6**, 1287–1314, <https://doi.org/10.5194/amt-6-1287-2013>.
- , and Coauthors, 2015: Dust aerosol radiative effects during summer 2012 simulated with a coupled regional aerosol–atmosphere–ocean model over the Mediterranean region. *Atmos. Chem. Phys.*, **15**, 3303–3326, <https://doi.org/10.5194/acp-15-3303-2015>.
- Nisantzi, A., R. E. Mamouri, A. Ansmann, G. L. Schuster, and D. G. Hadjimitsis, 2015: Middle East versus Saharan dust extinction-to-backscatter ratios. *Atmos. Chem. Phys.*, **15**, 7071–7084, <https://doi.org/10.5194/acp-15-7071-2015>.
- Pace, G., D. Meloni, and A. di Sarra, 2005: Forest fire aerosol over the Mediterranean Basin during summer 2003. *J. Geophys. Res.*, **110**, D21202, <https://doi.org/10.1029/2005JD005986>.
- , A. di Sarra, D. Meloni, S. Piacentino, and P. Chamard, 2006: Aerosol optical properties at Lampedusa (central Mediterranean). 1. Influence of transport and identification of different aerosol types. *Atmos. Chem. Phys.*, **6**, 697–713, <https://doi.org/10.5194/acp-6-697-2006>.
- Peuch, V.-H., M. Amodei, T. Barthet, M.-L. Cathala, B. Josse, M. Michou, and P. Simon, 1999: MOCAGE: Modèle de Chimie, Atmosphérique à Grande Echelle. *Actes des Atelier de Modélisation de l'Atmosphère AMA1999*, Toulouse, France, Météo-France, 33–36.
- Randel, W. J., and M. Park, 2006: Deep convective influence on the Asian summer monsoon anticyclone and associated tracer variability observed with Atmospheric Infrared Sounder (AIRS). *J. Geophys. Res.*, **111**, D12314, <https://doi.org/10.1029/2005JD006490>.
- Ricaud, P., and Coauthors, 2014: Impact of the Asian monsoon anticyclone on the variability of mid-to-upper tropospheric methane above the Mediterranean Basin. *Atmos. Chem. Phys.*, **14**, 11 427–11 446, <https://doi.org/10.5194/acp-14-11427-2014>.
- Rothman, L. S., and Coauthors, 2013: The HITRAN2012 molecular spectroscopic database. *J. Quant. Spectrosc. Radiat. Transfer*, **130**, 4–50, <https://doi.org/10.1016/j.jqsrt.2013.07.002>.
- Sahu, L. K., S. Lal, and S. Venkataramani, 2006: Distributions of O₃, CO and hydrocarbons over the Bay of Bengal: A study to assess the role of transport from southern India and marine regions during September–October 2002. *Atmos. Environ.*, **40**, 4633–4645, <https://doi.org/10.1016/j.atmosenv.2006.02.037>.
- Scheeren, H. A., and Coauthors, 2003: The impact of monsoon outflow from India and Southeast Asia in the upper troposphere over the eastern Mediterranean. *Atmos. Chem. Phys.*, **3**, 1589–1608, <https://doi.org/10.5194/acp-3-1589-2003>.
- Seibert, P., and A. Frank, 2004: Source-receptor matrix calculation with a Lagrangian particle dispersion model in backward mode. *Atmos. Chem. Phys.*, **4**, 51–63, <https://doi.org/10.5194/acp-4-51-2004>.

- Shohami, D., U. Dayan, and E. Morin, 2011: Warming and drying of the eastern Mediterranean: Additional evidence from trend analysis. *J. Geophys. Res.*, **116**, D22101, <https://doi.org/10.1029/2011JD016004>.
- Sić, B., L. El Amraoui, V. Marécal, B. Josse, J. Arteta, J. Guth, M. Joly, and P. D. Hamer, 2015: Modeling of primary aerosols in the chemical transport model MOCAGE: Development and evaluation of aerosol physical parameterizations. *Geosci. Model Dev.*, **8**, 381–408, <https://doi.org/10.5194/gmd-8-381-2015>.
- Stein, A. F., R. R. Draxler, G. D. Rolph, B. J. B. Stunder, M. D. Cohen, and F. Ngan, 2015: NOAA's HYSPLIT atmospheric transport and dispersion modeling system. *Bull. Amer. Meteor. Soc.*, **96**, 2059–2077, <https://doi.org/10.1175/BAMS-D-14-00110.1>.
- Stohl, A., C. Forster, A. Frank, P. Seibert, and G. Wotawa, 2005: Technical note: The Lagrangian particle dispersion model FLEXPART version 6.2. *Atmos. Chem. Phys.*, **5**, 2461–2474, <https://doi.org/10.5194/acp-5-2461-2005>.
- Thieuleux, F., C. Moulin, F.-M. Bréon, F. Maignan, J. Poitou, and D. Tanré, 2005: Remote sensing of aerosols over the oceans using MSG/SEVIRI imagery. *Ann. Geophys.*, **23**, 3561–3568, <https://doi.org/10.5194/angeo-23-3561-2005>.
- Thouret, V., A. Marenco, J. A. Logan, P. Nédélec, and C. Grouhel, 1998: Comparisons of ozone measurements from the MOZAIC airborne program and the ozone sounding network at eight locations. *J. Geophys. Res.*, **103**, 25 695–25 720, <https://doi.org/10.1029/98JD02243>.
- Wargan, K., S. Pawson, M. A. Olsen, J. C. Witte, A. R. Douglass, J. R. Ziemke, S. E. Strahan, and J. E. Nielsen, 2015: The global structure of upper troposphere-lower stratosphere ozone in GEOS-5: A multiyear assimilation of EOS *Aura* data. *J. Geophys. Res. Atmos.*, **120**, 2013–2036, <https://doi.org/10.1002/2014JD022493>.
- Ziemke, R., and Coauthors, 2014: Assessment and applications of NASA ozone data products derived from *Aura* OMI/MLS satellite measurements in context of the GMI chemical transport model. *J. Geophys. Res. Atmos.*, **119**, 5671–5699, <https://doi.org/10.1002/2013JD020914>.
- Ziv, B., H. Saaroni, and P. Alpert, 2004: The factors governing the summer regime of the eastern Mediterranean. *Int. J. Climatol.*, **24**, 1859–1871, <https://doi.org/10.1002/joc.1113>.

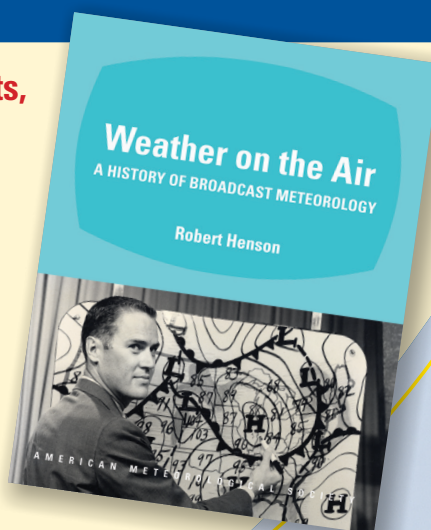
From roots in radio to graphics-laden TV segments, this history is an entertaining read for anyone fascinated by the public face of weather!

Weather on the Air: A History of Broadcast Meteorology

ROBERT HENSON

From low humor to high drama, *Weather on the Air* documents the evolution of weathercasts, including the people, technology, science, and show business that combine to deliver the weather to the public. Meteorologist and science journalist Robert Henson has combined decades of research, dozens of interviews, and historical photos to create the first comprehensive history of its kind, featuring:

- Entertainers, scientists, and the long-term drive to professionalize weathercasting
- The complex relations between government and private forecasters
- How climate change science and the Internet have changed the face of today's broadcasts



© 2010, HARDCOVER, 248 PAGES

ISBN: 978-1-878220-98-1

AMS CODE: WOTA

LIST \$35 MEMBER \$25

AMS BOOKS

RESEARCH APPLICATIONS HISTORY

www.ametsoc.org/amsbookstore